



Thermal conduction in a 2-D FCT plasma hydrodynamic code

F. Reale¹

Istituto e Osservatorio Astronomico, Palazzo dei Normanni, 90134 Palermo, Italy

Received 20 October 1994

Abstract

This paper presents an algorithm for inclusion of thermal conduction in a 2-D hydrodynamic code for compressible inviscid plasmas. The code is flexible for a wide series of applications in astrophysics, solves the hydrodynamic equations in conservative form in the most used coordinate systems and is based on an explicit fully 2-D flux corrected transport technique (FCT). The algorithm separates the energy equation in two distinct sections, characterized by different integration time steps (*time splitting*). The dynamic section is solved with the usual FCT scheme; the thermal section is solved using an implicit alternating-direction numerical scheme, which ensures unconditional numerical stability. The formulation is such to describe the plasma energy evolution also in non-uniformly spaced grids and in different coordinate systems. A whole set of tests of increasing complexity are presented to check the accuracy of the code.

1. Introduction

A previous paper [1] has described a general 2-D hydrodynamic code flexible for a wide series of applications in astrophysics. It solves the hydrodynamic equations in conservative form in the most used coordinate systems and is based on an explicit fully 2-D flux corrected transport technique (FCT). It owes its wide generality and applicability to the different geometries which can be optionally selected, to its accuracy in the description of steep gradient regions and shocks, to the flexibility in including additional physical effects, and to a good efficiency for speed. The code performs well on an extensive set of demanding non-linear tests, which have allowed a fine tuning of the FCT numerical parameters for best accuracy.

The first application of the code was to study the thermal stability of radiatively-cooling isobaric perturbations inside isothermal stratified atmospheres [2].

The relative accuracy and efficiency for speed of the code has allowed the extensive exploration of the relevant space of the parameters and therefore the accurate definition of the boundary between thermal stability and instability, determined by the competition between radiative cooling and dynamic dissipative effects, like Kelvin–Helmoltz and Rayleigh–Taylor instabilities.

The present paper describes the extension of the 2-D FCT hydrodynamic code to include the description of plasma thermal conduction. Energy transport by conduction in a high temperature plasma is in fact very effective, due to the $T^{5/2}$ dependence of conductivity. The inclusion of thermal conduction cannot be simply obtained by a straightforward extension of the FCT explicit numerical scheme, i.e. the linear addition of new terms in the equations already solved by the code. The highly non-linear dependence on temperature does in fact require an implicit scheme to ensure unconditional numerical stability [3]. In the approach presented here the effect of thermal conduction is computed as a separate section of the energy equa-

¹ E-mail: reale@oapa.astro.unipa.it, FReale@solar.stanford.edu

tion, with its own characteristic integration time steps and using an alternating-direction implicit (ADI) numerical scheme. This “time-splitting” approach has allowed to maintain the structure of the original FCT code substantially unaltered.

The above mentioned ADI, FCT and time-splitting techniques are singularly well-known from specialized literature [3] but this code assembles them homogeneously for general 2-D geometries, thereby allowing to access a new segment of astrophysical plasma problems, the description of thermally-conducting plasma flows in multi-dimensional systems. An analogous approach has been mentioned, but with no application to actual plasma problems, by Malagoli et al. [4] for a 2-D code based on the Piecewise Parabolic Method. The present code has been tested against a whole series of problems, reported here in detail, and already applied in its full functionality to study how the thermal stability of stratified atmospheres is influenced by plasma thermal conduction [5].

The paper is organized as follows: Section 2 briefly reviews the FCT explicit scheme of the 2-D hydrodynamic code; Section 3 describes in detail the insertion of thermal conduction in the code; Section 4 reports on some testing on the upgraded code; conclusions are drawn in Section 5.

2. The FCT code

The code solves the equations of mass, momentum and energy conservation for a compressible fully-ionized non-viscous fluid:

$$\frac{\partial n}{\partial t} + \nabla \cdot (nv) = 0, \quad (1)$$

$$\frac{\partial (nv)}{\partial t} + \nabla \cdot (nvv) = -\frac{1}{m} \nabla p + \frac{\mathcal{Q}_F}{m}, \quad (2)$$

$$\frac{\partial u}{\partial t} + \nabla \cdot [(u+p)v] = \mathcal{Q}_F \cdot v + \mathcal{Q}_E, \quad (3)$$

where

$$u = \frac{1}{2} mnv^2 + \mathcal{E}, \quad p = (\gamma - 1) \mathcal{E},$$

and where $\gamma = 5/3$, n is the particle volume density, p the pressure, m is the average mass per particle ($m = 2.1 \times 10^{-24}$ g for solar abundance), v is the

plasma bulk velocity, \mathcal{Q}_F includes all relevant external forces, such as gravity, \mathcal{Q}_E all relevant thermal energy sources and losses, such as an external heating, radiative losses.

The numerical solution is based on an explicit fully two-dimensional Flux Corrected Transport scheme [6–10], with some improvements, and solves the fluid equations in conservative form, thus enforcing the conservation of quantities. Possible source terms are treated independently (e.g. [2]). The scheme consists first of a transport step, in which the density of any of the relevant physical quantities is transported according to the local velocity field. The transport is expressed as variation of the density in a cell due to opposite contributions of outflows and inflows in a time step. The inflows/outflows are computed as half-indexed quantities with respect to the coordinates, i.e. they are computed at the center of the side of the cell across which they flow. Therefore the values of velocity and density derive from an interpolation. In particular we average between the values at the two grid points bounding the side of the cell.

The cell areas and volumes appear only through multiplications and divisions in the whole code. This allows for a straightforward switching among different geometries. In particular we have implemented the 2-D geometries corresponding to all possible choices of 2-D Cartesian, cylindrical and spherical coordinate systems.

After transport, the quantities are artificially diffused in order to inhibit numerical instabilities and errors. This diffusion is partly compensated for by an explicit antidiffusion step, corrected with a non-linear numerical filter (the so-called *limiter*) which enforces local monotonicity of the solution and is tuned to provide the “best” balance between accuracy and stability (it is adjusted by testing the code on specific model problems for which the exact solution is known). More specifically, the code used here adopts Scheme C of Reale et al. [1], in which the limiter is a hybrid between the one devised by Zalesak [9] (see also Kössl and Müller [11]) and that originally developed by Boris and Book [6]. The diffusion (μ) and antidiffusion (ν) coefficients along each of the two directions are those suggested by Boris and Book [8]:

$$\mu = 1/6 + 1/3\epsilon^2, \quad \nu = 1/6 - 1/6\epsilon^2,$$

where

$$\epsilon = \Lambda v \frac{\Delta t}{\Delta \Omega}.$$

Δt is the integration time step, $\Delta \Omega$ is the local volume element centered on grid point, v is the component of the local velocity along one direction, Λ is the area element perpendicular to the flux direction, i.e. across which the flux flows.

As for the limiter, the code adopts the two-dimensional flux limiter devised by Zalesak [9] (see also [10]), and used also by Kössl and Müller [11], hybridized with the addition of the strong one-dimensional limiter of Boris and Book [6,8] as a “pre-limiting” step (see also [9]); the use of this limiter is possible only within a fully two-dimensional FCT approach.

The code is highly reliable for describing shocks and steep gradient density distributions and, in contrast with other FCT implementations, maintains fairly regular behavior in regions where fluid dynamical quantities are expected to vary smoothly. Moreover, this implementation of FCT enables one to use a relatively large Courant number (0.7 - 0.8).

In the full version of the code as described in Reale et al. [1], we repeat the whole procedure including the advection scheme, the diffusion and the antidiffusion steps twice for each time step, first for the half and then for the full time step [10], to ensure a second order accuracy in time integration. Later, however [2], we have introduced a small modification in order to increase the calculation speed: the antidiffusion stage is skipped in the calculation of quantities for the half time step. We have redone the 2-D hydrodynamic tests reported by Reale et al. [1] using this simplification, and have found that the results remain essentially unchanged, with a $\sim 40\%$ improvement in the calculation speed [2].

3. 2-D thermal conduction

The inclusion of thermal conduction (we use the formulation of Spitzer [12]) changes the energy Eq. (3) into:

$$\frac{\partial u}{\partial t} + \nabla \cdot [(u + p)\mathbf{v}] = \mathcal{Q}_F \cdot \mathbf{v} + \mathcal{Q}_E - \nabla F_c, \quad (4)$$

where

$$T = \frac{p}{2kn}, \quad F_c = -\kappa T^{5/2} \nabla T,$$

T is the temperature of the atmosphere, κ is the plasma thermal conductivity (assumed isotropic for simplicity in these expressions).

As mentioned before, this equation is solved in two separate phases, involving different numerical algorithms and different integration time steps (*time splitting*). One phase involves the evolution dictated by purely thermal processes, i.e. conduction, heating and energy losses, which usually occur over time scales shorter than the dynamic time scales. The corresponding equation can be written as a temperature equation:

$$\frac{\partial T}{\partial t} = \frac{\gamma - 1}{2nk} [-\nabla F_c + \mathcal{Q}_E]. \quad (5)$$

Then we have to take into account the dynamic evolution, occurring on larger time scales:

$$\frac{\partial u}{\partial t} + \nabla \cdot [(u + p)\mathbf{v}] = \mathcal{Q}_F \cdot \mathbf{v}. \quad (6)$$

Eq. (6) is solved with the usual modified FCT scheme, together with Eqs. (1) and (2), and the integrating time step is given by the Courant condition [3,13]:

$$\Delta t_{dy} \leq \frac{\Delta s}{|\mathbf{v}| + c_s}, \quad (7)$$

where Δs is the smallest of the two sides of a cell and c_s is the sound speed.

Eq. (5) is solved implicitly according to the method described in Richtmyer and Morton [3], which ensures unconditional numerical stability. In particular, if Eq. (5) is indicated schematically with the following functional form:

$$\frac{\partial f}{\partial t} = \sigma_x \frac{\partial^2 f^\alpha}{\partial x^2} + \sigma_y \frac{\partial^2 f^\alpha}{\partial y^2} + S(x, y), \quad (8)$$

where $f \equiv T$, x and y are generically the two orthogonal coordinates, σ_x , σ_y are the respective thermal conductivity coefficients, $\alpha = 7/2$ for our specific case, $S(x, y)$ indicates whatever source term outside the non-linear second order terms, the integration of Eq. (8) is carried out in two half time steps, according to the following finite difference representation:

$$\frac{f_{jk}^{n+1/2} - f_{jk}^n}{\Delta t}$$

$$= \frac{1}{2} \left[\frac{\sigma_x}{\Delta x^2} \delta_x^2 (f^\alpha)^{n+1/2} + \frac{\sigma_y}{\Delta y^2} \delta_y^2 (f^\alpha)^n \right] + \frac{1}{2} S_{jk}^n, \quad (9)$$

$$\frac{f_{jk}^{n+1} - f_{jk}^{n+1/2}}{\Delta t} = \frac{1}{2} \left[\frac{\sigma_x}{\Delta x^2} \delta_x^2 (f^\alpha)^{n+1/2} + \frac{\sigma_y}{\Delta y^2} \delta_y^2 (f^\alpha)^{n+1} \right] + \frac{1}{2} S_{jk}^{n+1/2}, \quad (10)$$

where $\delta_x^2 f = f_{j+1k} - 2f_{jk} + f_{j-1k}$ and $\delta_y^2 f = f_{jk+1} - 2f_{jk} + f_{jk-1}$, and, for the sake of simplicity, we have assumed a grid equispaced along the two directions, with cell sides Δx and Δy , respectively. Eq. (9), and equivalently Eq. (10), can then be solved by rearranging it in the form:

$$-A_{jk} w_{j+1k} + B_{jk} w_{jk} - C_{jk} w_{j-1k} = D_{jk}, \quad (11)$$

where

$$f_{jk}^{n+1/2} = f_{jk}^n + w_{jk}.$$

The solution of this tridiagonal system is:

$$w_{jk} = E_{jk} w_{j+1k} + F_{jk}, \quad (12)$$

where

$$E_{jk} = \frac{A_{jk}}{B_{jk} - C_{jk} E_{j-1k}},$$

$$F_{jk} = \frac{D_{jk} + C_{jk} F_{j-1k}}{B_{jk} - C_{jk} E_{j-1k}}.$$

This solution is implicit and unconditionally numerically stable [3] and, as clear from Eqs. (9) and (10), the method is an alternating-direction method.

The integration time step Δt_{en} in this section is ruled by the local characteristic times of conduction and energy sources. In particular we use:

$$\Delta t_{en} = \min(\Delta t_{cond}, \Delta t_Q),$$

where

$$\Delta t_{cond} = \frac{nk \Delta s^2}{(\gamma - 1) \kappa T^{5/2}},$$

Δs being the minimum between Δx and Δy , and

$$\Delta t_Q = \frac{P}{(\gamma - 1) Q'_E},$$

Q'_E being the most important among the energy source terms. As a further constraint, we also impose an upper limit (presently 10%) on the local variation of the temperature in a time step.

As mentioned above, in general $\Delta t_{en} \neq \Delta t_{dy}$, so that Eqs. (5) and (6) will be integrated on different time steps. In conditions of typical astrophysical systems we usually have $\Delta t_{en} \leq \Delta t_{dy}$. Therefore we match dynamic and energetic stages by counting as many Δt_{en} 's as necessary to cover a single Δt_{dy} , the last step in a sequence of energy integrations being given by the time difference to match exactly the dynamic time step. If it happens that $\Delta t_{en} > \Delta t_{dy}$, then the shorter time interval is used.

As for boundary conditions, we can now choose also either a fixed temperature or a zero temperature gradient, as boundary conditions on the energy equation.

In order to handle also non-uniformly spaced grids and different coordinate systems, we have simply generalized the expressions for the gradients and divergences in Eqs. (9) and (10) by expressing Δx_j and Δy_k as ratios of the corresponding cell volume and side area.

The flow chart of Fig. 1 shows how the code appears to be structured after the inclusion of plasma thermal conduction. The code can be conceptually seen as divided into three sections: a) initial conditions, b) thermal section, c) dynamic section. The first section concerns the selection and preparation of the initial configuration, of the boundary conditions, and of all the relevant parameters required to calculate the plasma evolution. The thermal section includes the implicit numerical scheme for the calculation of the thermal conduction, which is characterized by the thermal time step. As soon as the thermal integration time sum up to a single dynamic time step, dictated by the Courant condition, the code switches to the dynamic section. Here the FCT scheme is at work on the four conservation equations and the time step is the dynamic step.

The increment in computer time due to the execution of the new section of the code, the thermal conduction section, amounts to $\sim 30\%$ for systems in which the thermal time scale is equal to the dy-

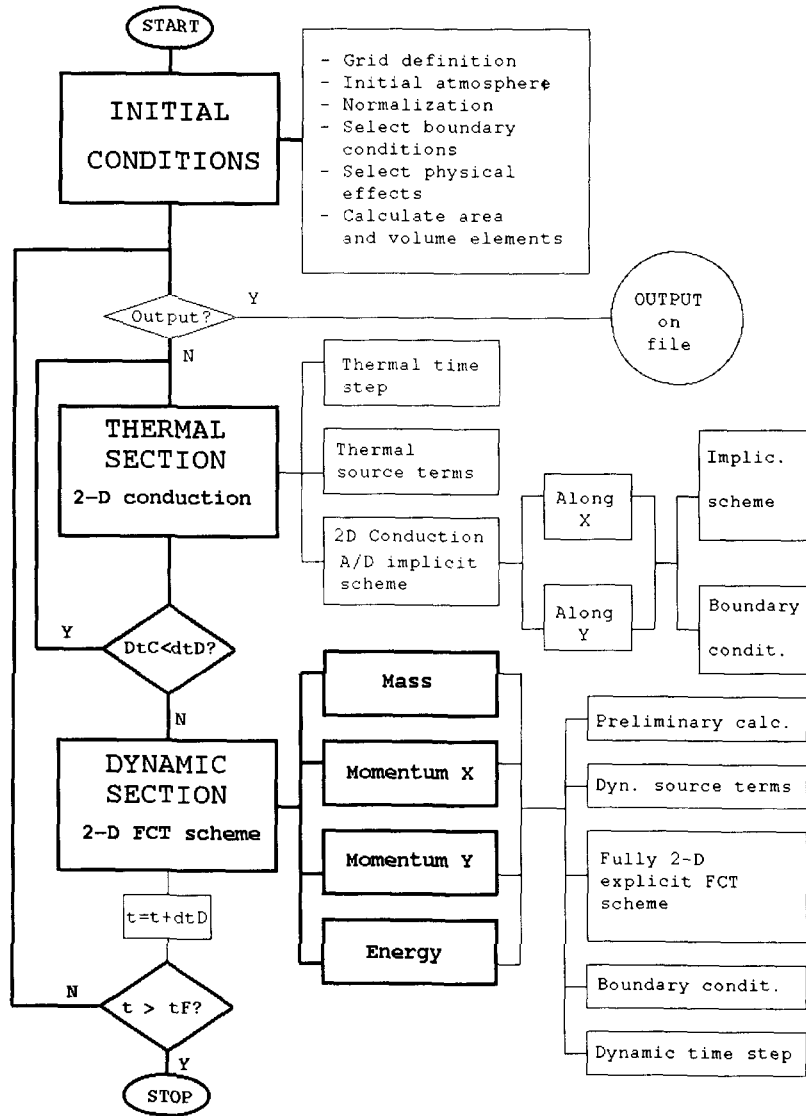


Fig. 1. Flow chart of the 2-D hydrodynamic code in the configuration including the description of plasma thermal conduction. We have identified three main sections (initial conditions, thermal section, dynamic section). We indicate with DtC the total integration time inside the thermal section and with dtD the dynamic time step. tF is the selected final time.

dynamic time scale. In general the expected shorter thermal time scales, which will strongly depend on the specific temperature conditions of the selected atmosphere, will further enhance the fraction of computer time spent in the conduction section. However, the time-splitting technique approach can be always considered as a time-saving approach, since we use several integration time steps tailored to the specific physical processes involved, instead of a single time step, namely the smallest one.

4. Testing

As done with the previous versions of the code, we have tested the upgraded code through the computation of problems with known solutions. We have considered gradually higher levels of complications, starting from pure conduction 1-D problems, therefore testing only the conduction section of the code, and ending with the evolution of spherical perturbations inside isothermal conducting atmospheres, for which analytic solutions are not available.

4.1. Pure conduction tests

In these tests the plasma is assumed permanently static and with a uniform and “frozen” density distribution. Therefore only thermal conduction across the plasma is considered, i.e. only Eq. (5) is solved.

4.1.1. Steady solutions

We have first to computed the evolution of the non-trivial plane parallel steady solution of a conducting plasma with fixed non-equal temperatures (T_0 , T_1) at two extremes ($s_0 = 0$, s_1 , where s can be either x or y Cartesian coordinates) of a Cartesian grid. The plasma is kept at uniform constant density and plasma dynamics is neglected. The steady-state distribution of temperature is:

$$T(s) = T_0 \left[\frac{(T_1/T_0)^{7/2} - 1}{s_1} s + 1 \right]^{2/7}. \quad (13)$$

The expected time-dependent solution of this problem is that the temperature distribution remains constant all the time. We have performed this test with the initial plane parallel profile along each of the two orthogonal

directions, with $T_0 = 10^5$ K and $T_1 = 10^7$ K at $s_1 = 10^{10}$ cm with 100 cells along the relevant direction. Zero-gradient boundary conditions are assumed along the direction orthogonal to s . Over ~ 4000 integration steps the solution does not change more than 10^{-6} with respect to the initial profile.

We have also performed the same test, with the same results, in a cylindrical coordinate system (r, θ) , where the analytic solution is:

$$T(r) = T_0 \left[\frac{(T_1/T_0)^{7/2} - 1}{\ln(r_1/r_0)} \ln(r/r_0) + 1 \right]^{2/7}. \quad (14)$$

4.1.2. Propagation of a plane pure conduction front

We have considered the propagation of a plane pure conduction front in a uniform high temperature plasma.

The equation solved for the propagation along the direction s is:

$$\frac{\partial T}{\partial t} = a \frac{\partial}{\partial s} \left(T^n \frac{\partial T}{\partial s} \right), \quad (15)$$

where $n = 5/2$ in our case.

For this problem an analytic solution is available as a self-similar solution [14], which can be found by setting:

$$\zeta = \frac{s}{aQ^n t^{1/(n+2)}}$$

as dimensionless parameter, where Q is the integral of T over the whole space. The solution is then given by:

$$T = T_c \left(1 - \frac{s^2}{s_f^2} \right)^{1/n}, \quad (16)$$

where

$$T_c = \left(\frac{Q^2}{at} \right)^{1/(n+2)} \left(\frac{n}{2(n+2)} \zeta_0^2 \right)^{1/n},$$

$$s_f = (aQ^n t)^{1/(n+2)} \zeta_0,$$

$$\zeta_0 = \left[\frac{(n+2)^{1+n} 2^{1-n}}{n\pi^{n/2}} \right]^{1/(n+2)} \times \left[\frac{\Gamma(1/2 + 1/n)}{\Gamma(1/n)} \right]^{n/(n+2)}$$

and Γ is the gamma function.

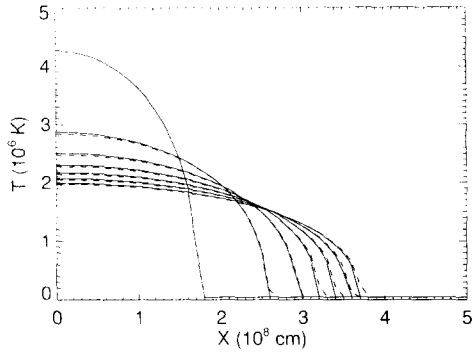


Fig. 2. Propagation (rightwards) of a plane parallel pure conduction front. Comparison of temperature distributions along the direction of propagation as computed numerically with the code described in the text (dashed lines), sampled every 0.5 s, with the corresponding analytic solutions (solid lines).

We have described the propagation of the front starting from the analytic solution at $t = 0.1$ s for a plasma with a density of 10^{10} cm^{-3} and with the integral of temperature $1.2 \times 10^{15} \text{ K cm}$, so that the maximum initial temperature is at $4.2 \times 10^6 \text{ K}$. Zero-gradient conditions on temperature are assumed at all boundaries. The propagation computed numerically is in good accord with the analytic solution, as shown in Fig. 2.

4.1.3. Propagation of a spherical pure conduction front

A test similar to the previous one is the description of the propagation of a spherical conduction front in a uniform plasma. In this case we can test the code for computations in a coordinate system different from the Cartesian.

Also for this problem it is possible to obtain an analytical solution:

$$T = T_c \left(1 - \frac{r^2}{r_f^2} \right)^{1/n}, \quad (17)$$

where

$$T_c = \frac{4}{3} \pi \zeta_1^3 \left[\frac{n \zeta_1^2}{2(3n+2)} \right]^{1/n} \frac{Q}{\frac{4}{3} \pi r_f^3},$$

$$r_f = (aQ^n t)^{1/(3n+2)} \zeta_1,$$

$$\zeta_1 = \left(\frac{3n+2}{2^{n-1} n \pi^n} \right)^{1/(3n+2)}$$

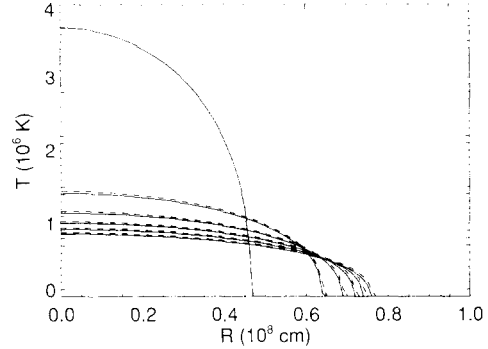


Fig. 3. Propagation of a spherical pure conduction front. Comparison of temperature distributions along the radial direction as computed numerically with the code described in the text (dashed lines), sampled every 1 s, with the corresponding analytic solutions (solid lines).

$$\times \left[\frac{\Gamma(5/2 + 1/n)}{\Gamma(1 + 1/n) \Gamma(3/2)} \right]^{n/(3n+2)}.$$

We have computed the numerical solution in a spherical coordinate system (r, θ) , taking as initial profile the analytical solution at $t=0.05$ s, for $Q = 10^{30} \text{ K cm}^3$ and density 10^{10} cm^{-3} . The grid is 101×21 cells, with $0 < r < 10^8 \text{ cm}$ and $0 < \theta < \pi/2$. The resulting propagation, compared with the analytical solution, is reported in Fig. 3.

4.2. Tests with both thermal conduction and plasma hydrodynamics

4.2.1. Propagation of a plane parallel conduction front

Now we describe the propagation of a plane conduction front including also the plasma hydrodynamics. Therefore this is no more a pure conduction front, but the propagation is complicated by the presence of the plasma dynamics, and the code is now tested in its full functionality, i.e. the whole set of Eqs. (1), (2) and (4) are solved, in particular with $Q_F = 0$ and $Q_E = 0$. We take as initial conditions the same as in Section 4.1.2. Since the density distribution of the plasma is initially uniform, the presence of a thermal front implies also the presence of a strong pressure wave which will eventually determine a significant plasma motion in the same direction as the conduction front. In Fig. 4 we report results for this test in terms of temperature, particle density, pressure and veloc-

ity distributions along the direction of propagation at some selected times during the first 3 s of propagation. If we look at Fig. 2, we notice that the conduction front propagates through $\sim 2 \cdot 10^8$ cm in 3 s. The mean propagation speed is therefore ~ 700 km/s during that time, much larger than the mean plasma sound speed (for $T \sim 2 \cdot 10^6$ K, $c_s \sim 200$ km/s). This means that we are still in conditions for which the front propagates almost as a pure conduction front and that we can still compare the numerical solution with the analytic solution of Eq. (15). Of course, we expect a detachment from the analytic solution as soon as the conduction speed is significantly reduced and approaches the plasma local sound speed, i.e. when the front temperature is reduced significantly from the initial high value. Indeed we see in Fig. 4d that the local plasma velocity increases with time, although well below the sound speed. Also the density begins to change significantly at late times (Fig. 4b), when a density front is forming, as a consequence of the pressure front. At late times the conduction front computed numerically propagates slightly faster than in the analytic solution because of the additional shift due to the plasma bulk motion.

4.2.2. Propagation of a cylindrical conduction front

In this test we have taken advantage of the possibility to switch easily among different coordinate systems. We have computed the propagation of a cylindrical conduction front in a plasma in two different geometric grid systems, so that we could compare two sets of numerical results obtained independently for the same problem, and check if they are self-consistent. In particular we have described the propagation both in a cylindrical coordinate system (r and θ) and in a Cartesian coordinate system. In the former the evolution is effectively a 1-D propagation along the radial direction, similarly to the test in Section 4.1.3. In the Cartesian coordinate system this is instead a proper 2-D problem, with radial symmetry with respect to the origin. We have taken as initial configuration a plasma with uniform density (10^9 cm $^{-3}$) and the same temperature distribution as in Section 4.1.2 along the radial direction r . We have followed the front propagation for 3.3 s.

In the test with the cylindrical coordinate system the grid is 150×10 cells (along θ a fine resolution

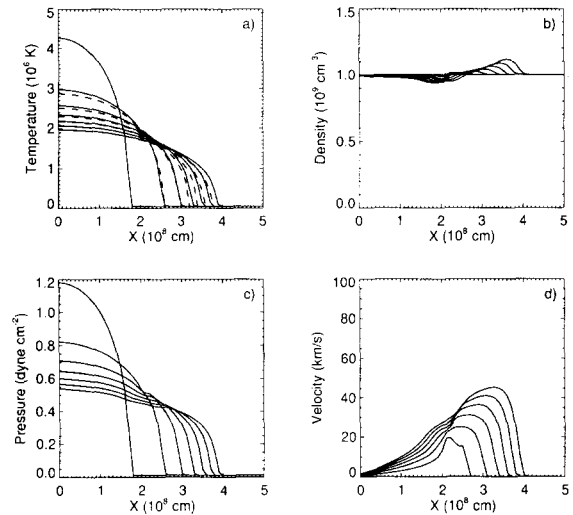


Fig. 4. Propagation of a plane parallel conduction front including the description of the plasma hydrodynamics. Temperature (a) (dashed = analytic, solid = numerical), density (b), pressure (c), velocity (d) distributions sampled every 0.5 s are reported (cf. Fig. 2).

is not necessary), with $0 < r < 1.5 \times 10^8$ cm and $0 < \theta < \pi/2$. The Cartesian grid is a square grid of 150×150 cells. In both cases we have set zero-gradient boundary conditions at all boundaries.

In Fig. 5 we compare the results at sampled times along the radial direction of the computation in cylindrical geometry (solid lines) to the one in Cartesian geometry (dashed lines). We find a generally satisfying accord between the two different computations. As evident from the temperature distributions the thermal front propagates at the same speed in the two cases, the temperature being slightly lower in the Cartesian computation. The front speed is the same also for density, pressure and velocity fields. The most significant difference between the results in the two cases is in the density distribution at the final time. In fact the peak of the rightward density front is higher (but by only 10%) in the Cartesian case than in the cylindrical case. This difference is to be ascribed to the different grid systems used which necessarily imply a different spatial resolution, which influences especially the description of spikes.

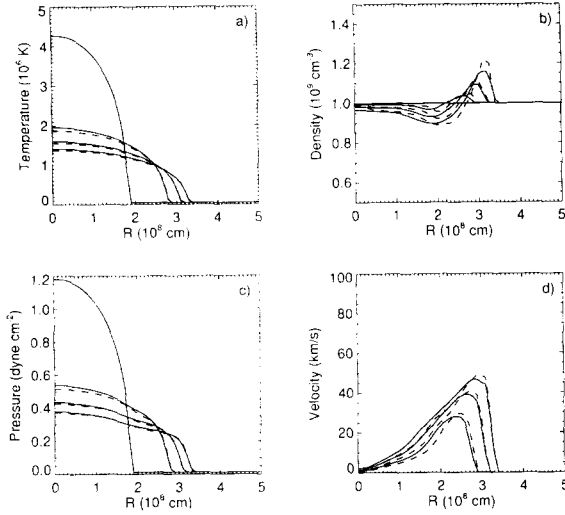


Fig. 5. Propagation of a cylindrical conduction front including plasma hydrodynamics computed with the same 2-D code but using two different coordinate systems, cylindrical (r, θ , solid lines) and Cartesian (dashed lines). Temperature (a), density (b), pressure (c) and velocity (d) distributions along the radial direction sampled every 1.1 s since $t = 0$ are reported.

4.2.3. Steady hydrostatic atmosphere

We have checked for the stability of a hydrostatic coronal loop as computed according to the static model of Serio et al. [15]. The atmosphere is derived by solving the detailed *time-independent* mass, hydrostatic and energy equations, including the effects of gravity, thermal conduction, and radiative losses from an optically thin plasma with solar abundance, and with a term of uniform steady heating. The temperature in the corona is above 10^6 K and decreases downwards to the solar surface with increasing steepness. A very steep transition region links the corona to the chromosphere. The base of the transition region has been carefully matched together to a model chromosphere taken from the models of Vernazza, Avrett and Loeser [16]. The chromosphere is in hydrostatic equilibrium with the upper atmosphere, and its energy balance is ensured by an “ad hoc” temperature-dependent heating function [17]. In other words, the steady-state heating function is uniform in corona and transition region, and non-uniform and temperature dependent in the chromosphere ($T < 20000$ K). Such heating function ensures the unconditional global thermal stability of the atmosphere [17].

As a test for the code we have let the atmosphere evolve from the hydrostatic state computed with the time-independent model. The specific momentum and energy equation solved for this problem are:

$$\frac{\partial (nv)}{\partial t} + \nabla \cdot (nvv) = -\frac{1}{m} \nabla p + ng, \quad (18)$$

$$\begin{aligned} \frac{\partial u}{\partial t} + \nabla \cdot [(u+p)v] \\ = mng \cdot v - n^2 P(T) + \mathcal{H}(r) + \nabla F_c, \end{aligned} \quad (19)$$

where the temperature dependence of the radiative losses function is a piece-wise power law $P(T) = \beta T^\alpha$, where the constants β and α assume different values in different temperature ranges, as prescribed in Rosner et al. [18], \mathcal{H} is the local heating function, assumed independent of time, built in such a way as to maintain steady the initial atmosphere, balancing the energy loss terms, like the radiative losses.

In this case we have considered a cylindrical coordinate system: the vertical Z and the radial r coordinate; therefore we assume rotational symmetry around the Z -axis and a logarithmic grid spacing along Z . In particular the smallest grid cell is at the base of the transition region and the spacing increases both going upwards (transition region and corona) and downwards (chromosphere) from there. The grid is equally and roughly spaced along r since we expected, and indeed obtained, a plane parallel evolution of the atmosphere. As boundary conditions we have fixed all quantities at the lower and upper boundaries of the atmosphere, and zero-gradient conditions at the outer boundaries.

As a result of the time-dependent computations, we expected the atmosphere to relax toward a steady state, at least almost hydrostatic, similar, but not identical, to the initial state, since the hydrostatic model had been computed on a different grid than the one used in the time-dependent numerical model. As a result, Fig. 6 shows a section along the Z -axis of the temperature, density, pressure and velocity distributions at the beginning and after 1000 s of evolution of a loop with a pressure 3 dyne cm^{-2} at the base of the transition region. This is a reasonably long time with respect to the conduction propagation time and to the radiative cooling time. The distributions of temperature, density and pressure show practically no evolution. The velocity field is affected by some numerical noise, especially at the interface between the chromosphere and

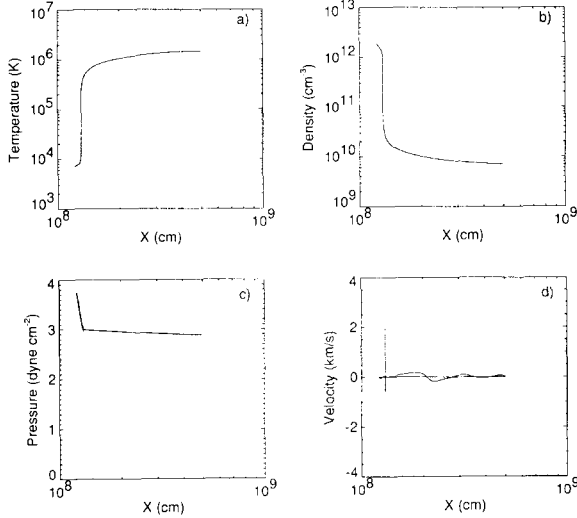


Fig. 6. Stability of a hydrostatic coronal loop atmosphere; section along the Z -axis of the temperature, density, pressure and velocity distribution at the beginning and after 1000 s of evolution of a loop with a pressure 3 dyne cm^{-2} at the base of the transition region.

the corona, which, however, is very steady and only a few percent of the speeds typical of coronal plasma motions.

4.2.4. Evaporation of an isobaric spherical condensation

As a final test we have considered a fully 2-D computation including hydrodynamics and isotropic thermal conduction. We have described the evolution of a spherical isobaric condensation initially set up inside an otherwise isothermal and uniform plasma. The unperturbed initial plasma is at temperature $T_0 = 10^6 \text{ K}$ and density $\rho_0 = 10^9 \text{ cm}^{-3}$, and is static.

We have considered a spherical uniform condensation with a density contrast $\delta = (\rho - \rho_0)/\rho_0 = 0.1$ and a radius $R = 10^8 \text{ cm}$. The grid is a cylindrical grid (z, r) with 150×50 cells of size $\Delta r = \Delta z = 10^7 \text{ cm}$. We have described only half of the relevant space, since the evolution is symmetric with respect to the Z -axis. Therefore the center of the perturbation is located at $r = 0$ and we have posed the radial speed $v_r = 0$ at $r = 0$. At the other boundaries we have set zero-gradient conditions for all quantities.

Since the perturbation is isobaric, the temperature inside the perturbation is initially 10% lower than outside. In the absence of major pressure forces the evo-

lution of the system will be governed mainly by the plasma thermal conduction. Heat will be transported inwards from outside to the center of the perturbation, so to reduce the temperature gap. The perturbation gradually expands (because the temperature gradient will propagate outwards) isotropically, but its intensity decreases, until it will eventually fade out. The characteristic time of the evolution is given by the conduction time:

$$\tau_c = \frac{\gamma}{\gamma - 1} \frac{pl^2}{2\kappa T^{7/2}} = 1.4 \times 10^6 \frac{pl^2}{T^{7/2}}, \quad (20)$$

where p is the local pressure and l represents the characteristic length of temperature variation, e.g. the size of the perturbation. If we take $\kappa = 9.2 \times 10^{-7} \text{ erg cm}^{-1} \text{ s}^{-1} \text{ K}^{-7/2}$ as the conduction coefficient, we obtain $\tau_c \approx 3.3 \text{ s}$. During this time, shorter than sonic propagation times, a pressure excess will develop inside the perturbation and this will determine a further dynamic expansion of the perturbation, and therefore a radial motion.

In Fig. 7 we report images of the temperature contrast $((T - T_0)/T_0)$ in absolute value with respect to the background plasma in the first 3 seconds of evolution, and the velocity field. The evolution follows the expected pattern in the expected times. The isotropic expansion and attenuation of the temperature perturbation is evident. The maximum temperature contrast decreases from 0.1 to 0.025 in 3 s. The radial velocity field is also visible with speeds of the order of a few km/s.

5. Conclusions

This paper presented an algorithm to include the description of plasma thermal conduction according to Spitzer [12] in a 2-D hydrodynamic code for compressible inviscid plasmas using the Flux Corrected Transport technique. The code was developed mostly for astrophysical applications, such as cooling flows in halos of clusters of galaxies, accretion disks, jet structures. The introduction of the description of plasma thermal conduction allows to study in detail coronal structures and in general systems where magnetic fields are able to funnel energy transport. Conduction is taken into account by the addition of a new section to the code using an implicit alternating-direction

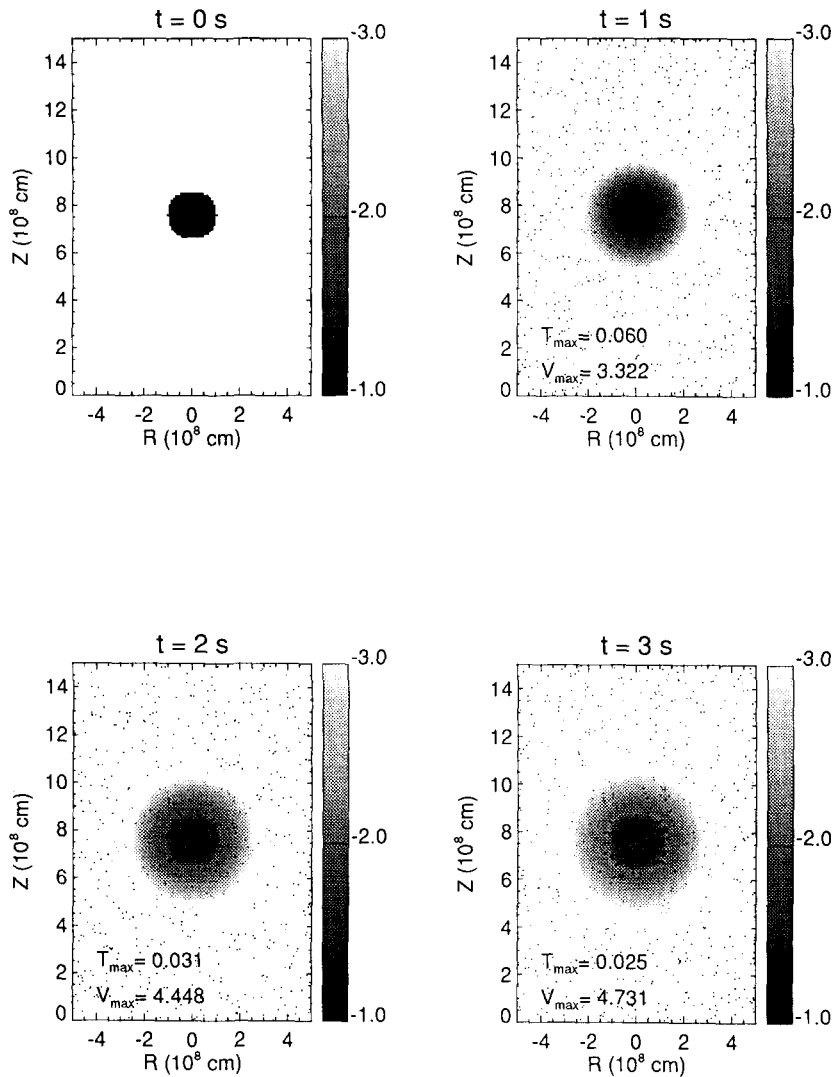


Fig. 7. Evolution of an isobaric spherical condensation inside a uniform isothermal atmosphere, under the effect of inward thermal conduction from the hotter surrounding atmosphere. The unperturbed plasma is static, with temperature 10^6 K and density 10^9 cm $^{-3}$. The perturbation is initially 10% cooler than the unperturbed plasma. We report grey-scale images, at the labelled times, of the logarithm of the temperature contrast above the background atmosphere. The velocity field is also reported as arrows whose lengths are scaled to the maximum speed reported in each image (km/s). For each image at $t > 0$ we report also the maximum temperature contrast in absolute value.

numerical scheme totally different from the FCT explicit scheme adopted for the description of the plasma pure hydrodynamics. The extension of the code has been quite straightforward by means of a technique of *time splitting* solving separately the dynamic and thermal sections of the energy equation. This technique allows also a saving of computing time because the dynamic and thermal sections are integrated on different time steps. Although the numerical techniques used are well known, this code assembles them homogeneously and allows to study quite complex problems, like the stability of multidimensional solar coronal structures [2,5]. We have also presented a whole set of tests, with which we could verify the validity and accuracy of the code in its various sections.

Acknowledgements

I would like to thank S. Serio for useful suggestions and G. Peres for help in the numerical implementation of the code. Ministero dell'Università e della Ricerca Scientifica e Tecnologica and Consiglio Nazionale delle Ricerche/Gruppo Nazionale di Astronomia are acknowledged for partial support.

References

- [1] F. Reale, G. Peres and S. Serio, *Nuovo Cimento B* 105 (1990) 1235.
- [2] F. Reale, R. Rosner, A. Malagoli, G. Peres and S. Serio, *Mon. Not. R. Astron. Soc.* 251 (1991) 379.
- [3] R.D. Richtmyer and K.W. Morton, *Difference Methods for Initial-Value Problems* (Interscience, New York, 1967).
- [4] A. Malagoli, R. Rosner and B. Fryxell, *Mon. Not. R. Astron. Soc.* 247 (1990) 367.
- [5] F. Reale, S. Serio and G. Peres, *Astrophys. J.* (1994) in press.
- [6] J.P. Boris and D.L. Book, *J. Comput. Phys.* 11 (1973) 38.
- [7] J.P. Boris, D.L. Book and K. Hain, *J. Comput. Phys.* 18 (1975) 248.
- [8] J.P. Boris and D.L. Book, *J. Comput. Phys.* 20 (1976) 397.
- [9] S.T. Zalesak, *J. Comput. Phys.* 31 (1979) 335.
- [10] J.P. Boris, D.L. Book and S. Zalesak, in: *Finite-Difference Techniques for Vectorized Fluid Dynamics Calculations*, D. Book, ed. (Interscience, New York, 1981) p. 29.
- [11] D. Kössl and E. Müller, *Astron. Astrophys.* 206 (1988) 204.
- [12] L. Spitzer Jr., *Physics of Fully Ionized Gases* (New York, 1962).
- [13] P.J. Roache, *Computational Fluid Dynamics* (Hermosa, Albuquerque, 1967).
- [14] Y.B. Zel'dovich, Y.P. Raizer, W.D. Hayes, R.F. Probstein, *Physics of Shock Waves and High-Temperature Hydrodynamic Phenomena* (Academic Press, New York, 1967).
- [15] S. Serio, G. Peres, G.S. Vaiana, L. Golub, R. Rosner, *Astrophys. J.* 243 (1981) 288.
- [16] J.E. Vernazza, E.H. Avrett, R. Loeser, *Astrophys. J. Suppl.* 45 (1980) 619.
- [17] G. Peres, R. Rosner, S. Serio, G.S. Vaiana, *Astrophys. J.* 252 (1982) 791.
- [18] R. Rosner, W. Tucker and G.S. Vaiana, *Astrophys. J.* 220 (1978) 643.